rGO Coated Cotton Fabric and Thermoelectric Module Arrays for Efficient Solar Desalination and Electricity Generation

Ahmed Mortuza Saleque[1,2a,b], Amrit Kumar Thakur[3], R. Saidur[4a,b], Mohammad Ismail Hossain[1,5], Wayesh Qarony[6], Md Shamim Ahamed[7], Iseult Lynch[8a,b], Y. Ma[3], Yuen Hong Tsang[2a,b,*]

1.) Department of Electrical and Computer Engineering, University of California, Davis, CA 95616, USA

2a.) Department of Applied Physics, Photonic Research Institute, and Materials Research Center, The Hong Kong Polytechnic University, Hung Hom, Kowloon, Hong Kong

2b.) Shenzhen Research Institute, The Hong Kong Polytechnic University, 518057 Shenzhen, Guangdong, People's Republic of China

3.) Department of Mechanical Engineering, University of California, Merced, CA, 95343, USA

4a.) Research Center for Nano-Materials and Energy Technology (RCNMET), School of Engineering and Technology, Sunway University, Bandar Sunway, Petaling Jaya 47500, Selangor Darul Ehan, Malaysia

4b.) School of Engineering, Lancaster University, Lancaster LA1 4YW, UK

5.) Research & Development, Meta Materials Inc., Pleasanton, CA 94588, USA

6.) Department of Electrical Engineering and Computer Sciences, University of California, Berkeley, CA 94720, USA

7.) Department of Biological and Agricultural Engineering, University of California, Davis, CA 95616, USA

8a.) School of Geography, Earth and Environmental Sciences, University of Birmingham, Edgbaston, B15 2TT Birmingham, UK

8b.) Institute for Global Innovation, University of Birmingham, Edgbaston, B15 2TT Birmingham, UK

*.) Corresponding author.

E-mail address: yuen.tsang@polyu.edu.hk (Y. H. Tsang).

ABSTRACT

One promising solution to the freshwater crisis is solar-driven interfacial evaporation-based desalination. However, an alternate strategy is needed to address both water and energy shortages in parallel. Additionally, the disposal of desalination brine necessitates specific consideration while designing a sustainable solar interfacial desalination system. Herein, we demonstrate a single system that utilizes incident solar irradiance to produce interfacial steam using reduced graphene oxide (rGO) coated cotton fabric (CF) to desalinate seawater with an evaporation efficiency of 86.98%. The high thermal conductivity and excellent optical absorption of rGO contribute to the absorption of a broad solar spectrum. The system also produces 339.26 mW of electricity simultaneously by deploying commercially available thermoelectric generator (TEG) modules that use the squandered heat, increasing the overall system efficiency by 7.3%. The use of a custom-made power electronics module ensures operating at the maximum power point which has also been verified by computer simulation. Finally, hydrogen gas with zero carbon emission is produced by electrolyzing the seawater utilizing the electricity generated by the TEG module using solar-induced heat at a rate of 0.52 mmol/h. Converting brine into hydrogen and oxygen gas by electrolysis demonstrates a potential *in-situ* approach for desalination waste remediation.

Keywords: Solar energy, Desalination, rGO, 2D materials, Brine disposal.

1. INTRODUCTION

The shortage of freshwater resources is a growing global issue. With 1.3 billion people projected to live in water-scarce areas by 2025, the need for efficient and effective water management is becoming ever more pressing. As the water needs of a growing global population continue to outstrip available supplies, countries need to find new ways to conserve and protect this vital resource for future generations. Desalinating seawater can be seen as one of the solutions to deal with the shortage of freshwater resources. However, the conventional desalination approach requires an energy-intensive process such as reverse osmosis, which may lead to an increase in energy consumption with energy prices so volatile and supply disrupted, the recent alignment of economic, climate, and security priorities has started the shift towards more sustainable energy solutions. [1] Therefore, it is important to develop more energy-efficient and environmentally friendly desalination techniques to ensure that water resources can be conserved in the future, and to reduce the associated environmental demands.

The interfacial solar steam generation (ISSG) technique is often seen as the most sustainable way to desalinate seawater owing to its high energy conversion efficiency, scalability, and low cost. In this method, the photon energy from solar irradiation is converted into thermal energy to quickly heat up a thin layer of water thereby producing steam at an accelerated rate. To meet one of the primary requirements of ISSG, that of rapidly converting the water to steam, researchers have utilized many different nanomaterials to achieve higher optical absorption in recent years. Among the materials that have been explored, carbon-based materials [2–7], 2D materials [8–12], MXene [13–18], and semiconductor materials [19–21] have shown encouraging results. Although

higher photothermal conversion efficiency can be achieved by using various 2D materials owing to their thickness-dependent bandgap, there is a higher cost associated with the production and purification of these materials, which hinders large-scale application of the ISSG approach. To be considered viable, ISSG is required to produce 14-15 liters of fresh water daily for a family of 4 members [22], and thus a large photothermal evaporator area (2-3 m^2) is typically needed. The associated cost of fabricating a 2-3 m^2 photothermal evaporation area with expensive materials is not feasible for practical application. Moreover, ISSG systems often require a substrate material upon which various nanoparticles are deposited to enhance optical absorption. Wood[23], bamboo[24], luffa sponge[22], polyurethane sponge[25], cotton[26], hydrogel[27], Cu foam[8], aerogel[28], cloth[26], and others[29] are used as substrate materials for fabricating the photothermal evaporator. However, cotton fabric is recognized as a low-cost substrate material owing to its wide availability, low cost, excellent water uptake property, flexibility, and durability. Therefore, we propose to use reduced graphene oxide (rGO) coated cotton fabric (CF) as a solar photothermal material for desalinating seawater at an evaporation efficiency of 86.98%. rGO demonstrates superior optical absorption, high thermal conductivity, strength, and flexibility.[30,31] The stability of rGO, due to its layer structure, is advantageous for solar steam generation applications compared to other carbon-based materials. Moreover, the superior hydrophilicity of CF eases the design complexity as an additional water uptake mechanism is not needed. Herein, we propose that uncoated CF suspended from the photothermal evaporator surface to inside the bulk water will work as a water transport system facilitating evaporation. As minimizing heat loss is an important factor in realizing high-efficiency photothermal energy conversion, we propose to use

expanded polyethylene foam (EPE) surrounding the rGO-coated CF. EPE foam has high insulating properties, and therefore it can reduce the radiative heat loss from the photothermal evaporator. There are a few demonstrations of using cotton cloth for desalination application. Previously candle soot-coated cotton cloth[32], MoS_2-coated cotton fabrics[33], aerogel[34], 2D materials[35] and activated carbon decorated cloth[26] have been used for photothermal energy conversion and desalination application. However, none of these are feasible for large-scale implementation owing to the complexity of extracting large amounts of candle soot and the higher cost associated with MoS_2 and activated carbon nanomaterials. The proposed rGO-coated CF is scalable, provides higher evaporation efficiency than current approaches, and has a facile fabrication process.

A further challenge to the widespread application of ISSG is the considerable percentage of solar heat that is wasted in solar-driven interfacial steam-producing devices despite improvements in optical, thermal, and water management.[36–38] There is room for further improvement of heat utilization by co-generating photothermal-induced steam and electricity. Thus, water shortage and energy deficit might be simultaneously addressed by combining solar desalination and electricity production.

In a previous study, P. Xiao et al. showcased the utilization of carbon nanotubes (CNTs)-based paper in conjunction with polydimethylsiloxane (PDMS) to harness electricity from directional water flow, achieving a maximum output power of 2.1 μW.[39] Notably, the inclusion of PDMS was observed to reduce the water transmission channels, as indicated by the authors. Likewise, Y. Xu et al. adopted an evaporation-driven electricity (EDE) generation technique, employing a 3D porous hydrophilic graphene aerogel (HGA), which

resulted in a continuous output voltage of 0.84 V and a maximum power density of 6.84 $\mu W\ cm^{-2}$.[40] In the EDE method, the generation of heat from solar energy induces a thermodiffusion effect, propelling hydrated ions carrying a countercharge toward the surface, where they accumulate at one end, following the flow direction, and establishing an ion concentration gradient, consequently forming potential difference.[41] However, it's worth noting that this method yields comparatively lower electricity generation and is cost-prohibitive for large-scale applications.

Herein, utilizing a commercially available thermoelectric generator (TEG) module, we demonstrate the generation of electricity from waste radiative heat in tandem with solar desalination using rGO coated CF. To achieve higher energy conversion efficiency, a thermal heat sink is employed at the cold side of the TEG module to provide a thermal barrier prior to adding the rGO coated CF. We use 15 TEG modules and thermal heat sink connected in series-parallel combination which generate 339.26 mW of electricity in parallel with solar desalination under 1 kW/m^2 solar irradiance. The conversion of electricity from the radiative heat produced by the ISSG system increases the overall energy conversion efficiency by 7.3%.

Additionally, the high salinity of desalination brine, a by-product of the solar interfacial desalination system, poses a challenge to its disposal.[42] The health of marine ecosystems is jeopardized when high-salinity brine is dumped into natural waters like rivers, lakes, or oceans.[43–45] It follows that the brine must be treated with a different strategy. However, the electrolysis of brine produces hydrogen and oxygen gas, which could be used to solve the disposal problem. The salt components are deposited at the electrodes and at the bottom of the electrolysis apparatus while the water is converted

6

into hydrogen and oxygen gas, making electrolysis a relatively inexpensive technique for removing the water from the brine. The deposited salt can be further processed for various applications. Accordingly, we also demonstrate the feasibility of electrolyzing the brine and generating hydrogen gas using the electricity generated by the TEG modules. Hydrogen gas is produced at a rate of 0.52 mmol/h using an electrolysis-based hydrogen generating system driven by 15 TEG modules. This might be a viable *in-situ* process for remediating the desalination waste. Moreover, the generated hydrogen gas can be stored in cylinders for later uses in many applications such as electricity generation from fuel cell, ammonia production or methanation. Recently hydrogen energy storage has shown its capacity to hasten the carbon-neutral global energy transition.[46,47] Due to the intermittent nature of solar energy, it is often required to store energy to ensure continuity of renewable energy-based systems. However, storing energy in the form of electrical energy using a battery pack is often seen as an expensive option with adverse environmental and ecological impacts from battery electrodes and chemicals during production and disposal.[48,49] Therefore, the storage of excess electrical energy generated from solar thermal systems in the form of hydrogen, rather than stored in a battery pack, is a sustainable option. In light of this, we demonstrate the generation of hydrogen gas from the electrolysis of brine utilizing electricity generated by TEG modules, simultaneously addressing the issue of brine disposal while also eliminating the requirement for a battery pack for energy storage. Furthermore, electrolysis has emerged as an important option for lowering the cost of manufacturing hydrogen.[50,51] The hydrogen electrolysis process produces no greenhouse gas emissions since the electricity is provided by the TEG module in the proposed system utilizing heat from the

incident solar irradiation. Hydrogen produced by electrolysis may be stored in metallic cylinders at low pressure for use at a later time. Storing hydrogen at low pressure is safer than storing liquified natural gas (LNG) or methane in cylinders.[52,53]

We demonstrate the co-generation of freshwater and power in this study utilizing a single system. The rGO-coated CF has an evaporation rate and efficiency of 1.385 kg m^{-2} h^{-1} and 86.98% while producing 339.26 mW of electricity from 15 TEG modules utilizing the radiated heat generated by the ISSG system. The overall system efficiency has been increased by 7.3% by converting waste heat to electricity. Finally, an electrolysis device driven by the electricity from the TEG modules generates H_2 gas at a rate of 0.52 mmol/h, which might be a viable option for desalination waste remediation.
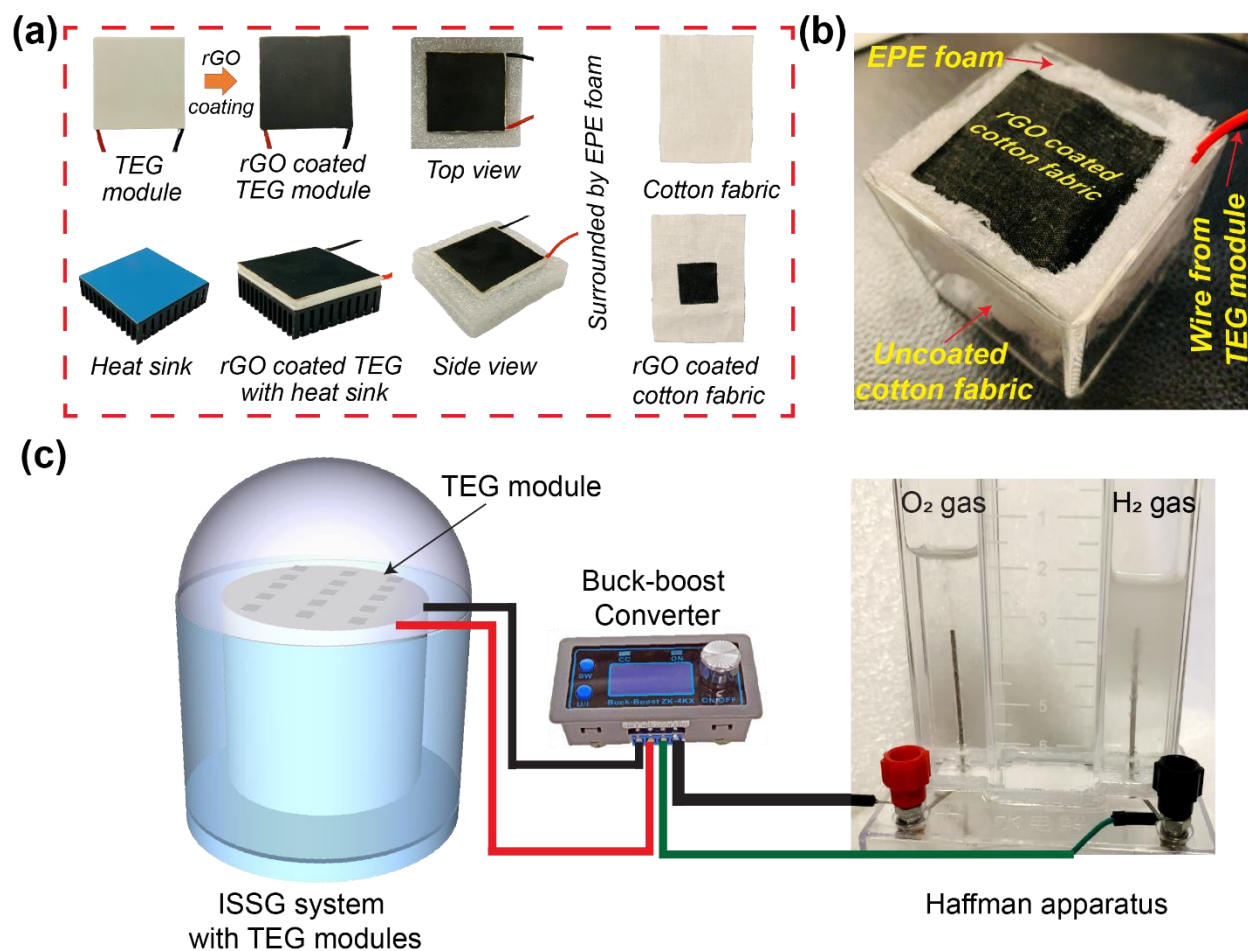
Figure 1. (a) Preparation of rGO coated cotton fabric (CF) and the thermoelectric generation (TEG) module with heat sink; (b) The photothermal water evaporation device structure. (c) Hydrogen gas generation from electrolysis of brine using the TEG module generated electricity.

2. Material and Methods

2.1 Materials and Characterization

Isopropyl alcohol (IPA) with 99.99% purity was acquired from J & K Scientific Ltd. (Guangzhou, China) and 0.4 wt% of graphene oxide dispersion (GO) was bought from Six Carbon Inc. (Beijing, China). No further purification of the compounds was performed before usage. Zhong Sheng Trade Co. supplied the extended polyurethane foam (EPE) with the following specifications: pore diameter of 300 nm; density of 25 kg/m^3; thickness

of 10 mm. A UV-Vis spectrometer (PerkinElmer Lambda 1050) was used to analyze the optical absorption spectra of the prepared samples. Scanning electron microscopy (SEM; TESCAN, VEGA3) with an acceleration voltage of 20 kV and equipped with energy-dispersive X-ray spectroscopy (EDX, INCA X-Act, Oxford) was used to characterize the microstructures of the as-prepared rGO coated CF. X-ray diffraction (XRD) patterns were acquired through Cu-K radiation using a diffractometer (Smart Lab, Rigaku) (40 kV, 100 mA).

2.2 Preparation of rGO coated CF

Prior to treatment, the CF were cleaned and ultrasonically washed followed by drying in an oven at 55 °C for 6 h. rGO was produced from graphite powder using a modified Hummer's method. According to this method, the graphite powder was heated in a muffle furnace at 485 °C at a heating rate of 4 °C min^{-1} for 2.5 hours. The hot side (top surface) of the TEG module was coated with rGO using a drop cast method covering an area of 16 cm^2 and followed by oven drying at 55 °C. The cold side of the same TEG module was intended to be submerged into the water during the solar desalination experiments. However, a commercially available heat sink made of copper is attached to the cold side of the TEG module to provide more insulation between the interfacial heating surface and the bulk water. Since heat can be radiated from the solar evaporation system, an extended polyurethane foam (EPE foam) was used to surround the heat sink connected TEG module. Another purpose of the EPE foam is to ensure that the heat sink connected to the TEG module floats on the water surface. Finally, it was wrapped by a polyurethane foam to reduce the radiative heat loss and make it float on the water. After that, the center area (4 cm × 4 cm) of the CF was coated with rGO to make rGO coated CF. The rGO

coated CF was kept in ambient temperature for drying. After drying, the rGO coated CF was carefully placed on top of the hot surface of the TEG module making sure that the rGO coated portion of the CF perfectly aligned with the rGO coated area of the TEG module. The rest of the uncoated white CF was inserted between the gap of the heat sink connected TEG module and the EPE foam. It was then bent downward to the bulk water so that the CF can transport water owing to its hydrophilicity. To access the performance improvement with the heat sink, another configuration was prepared following the same procedure but without attaching the heat sink on the cold side of the TEG module. Similarly, another configuration was prepared without using any rGO coating on the CF and TEG module. These three configurations were separately used for conducting solar evaporation experiments.

2.3 Solar evaporation, TEG voltage generation and hydrogen production experiments

All three different configuration were separately used for conducting the solar evaporation experiments. In the laboratory environment, the different configurations were separately illuminated with a xenon lamp (PLS-SXE300, Beijing Perfect Light Technology Co., Ltd) at 1 kW/m^2 solar irradiance. The mass losses over time were recorded every 10 seconds using a computer-connected electronic microbalance (Ohaus Corporation, CP213) and a power meter (THORLABS, S314C) to assess the solar irradiance. After that, the solar irradiance was varied from 1 to 3 kW/m^2 and the corresponding mass losses over time were recorded. The evaporation rate and efficiencies were calculated using the equations provided in Note S2 of the ESI. During the evaporation experiments, thermal images were captured at various instances using an IR camera (FLIR-E64501, Tallinn, Estonia, 2 °C

error range). <mark>A K-type thermocouple (Model: CENTER 306) with a data logging feature was used to measure the top and bottom surface temperature of the TEG module.</mark> The potential to harness the wasted heat has been investigated by generating heat-generated electricity via the Seebeck effect using a Thermoelectric generator (TEG) module. TEG modules were acquired from AliExpress. The TEG module is made of an n-type bismuth telluride (Bi_2Te_3) and a p-type Antimony telluride (Sb_2Te_3) semiconductors. The rGO-coated CF was mounted on the rGO-coated TEG module. This structure was encased with EPE foam to float and prevent heat loss. The TEG module was put in a beaker to perform solar evaporation experiments and measure voltage and current. The TEG generated voltage and current were measured using a digital multimeter (OWON 4 1/2 XDM1041). 15 TEG modules were connected in series-parallel combination to increase the voltage and current. All 15 TEG modules were contained in a 9 cm radius circular piece of EPE foam. The rGO coated CF (total rGO coated area 250 cm^2) was placed on top of the rGO coated TEG modules and the uncoated portion of the CF was inserted between the gap of the heat sink connected TEG module and the EPE foam as per the previously mentioned design. This configuration is placed in a quartz glass dome shaped structure as shown in **Figure 5**. Inside the dome-shaped construction were two compartments. The inner compartment held 2 liters of seawater collected from the Whampao harbour in Hong Kong, and the 15 TEG modules wrapped in EPE foam and covered with rGO coated CF were placed floating in it. When exposed to sunlight, the evaporated water condensed at the inner side of the dome-shaped structure, generating water droplets. The water droplets were gathered in the custom-built structure's outer compartment. A pipe was attached to discharge the accumulated water droplets from the

outer compartment, while another conduit supplied seawater to the inner compartment. The collected water was used to conduct ion concentration, pH, conductivity and TDS testing experiments using water quality testing equipment (model no. EZ-9909SP). Inductively coupled plasma mass spectrometry (ICP-MS) was employed to measure the Na^+, K^+, Ca^{2+} and Mg^{2+} ion concentrations in seawater and the desalinated water. The wastewater purification experiments were conducted using simulated wastewater prepared using 20 mg L^{-1} methylene blue (MB).

During the solar evaporation experiment, the temperature difference between the hot and cool surfaces of the TEG modules generated a voltage due to the Seebeck effect. The voltages generated by the TEG were delivered to the power electronics through two cables. The power electronics set-up is employed to ensure the maximum power extraction from the TEG module. A power converter (buck-boost) operating at a predetermined duty cycle has also been employed which has been carefully tuned to match the load resistance. The following steps were involved in matching the load resistance. Initially, the Thevenin equivalent resistance of the equivalent electrical circuit is computed to be 10.17 Ω, given that the internal resistance of each TEG module was determined to be 6.1 Ω. Now, according to the maximum power transfer theorem, the TEG modules will only deliver maximum power when the load resistance equals the Thevenin equivalent resistance determined value. The resistance of the Cu electrode immersed in seawater, which is measured to be 190.12 Ω, is regarded as the load resistance. Using the input-output power equation of the buck-boost converter, in conjunction with the calculated value of Thevenin equivalent resistance and the measured value of the load resistance, the duty cycle of the buck-boost converter in this

configuration is determined to be 81%. The detailed calculation and equations are provided in note S6 of the ESI.

Using MATLAB Simulink software, the electrical circuit with buck-boost converter was simulated. The electrical load resistance was varied in the simulation to obtain the corresponding current, voltage and power. The maximum power in the simulation environment matched to the experimentally obtained maximum power. The simulated circuit is provided in **Figure S7** (ESI). The output of the TEG modules is connected to the Cu electrode of the Hoffman apparatus (see Figure 5). The generated electricity electrolyzed brine, producing hydrogen and oxygen. The produced hydrogen gas can be stored in cylinders for use in various applications such as electricity generation using fuel cells, ammonia production, or methanation.

3. RESULTS AND DISCUSSION

A schematic illustration of the preparation process is presented in **Figure 1**. The rGO-coated CF was placed on top of a rGO-coated TEG module with a heat sink connected to its cold side. To reduce heat loss and maintain the structure floating on the water surface, EPE foam was utilized to surround it. Aside from the design shown in **Figure 1a**, two more configurations of the setup were constructed for the solar evaporation experiments. One configuration used uncoated CF and TEG modules, whereas the other used rGO-coated CF and TEG modules but no heat sink. The material and method section includes a detailed description of the setup and the solar evaporation experimental process.

Figures 2a and b show representative scanning electron microscopy (SEM) images of rGO-coated CF at different magnifications. **Figure 2a** demonstrates the presence of many microporous gaps, which are beneficial as they increase the water uptake capacity. The more detailed view in the SEM image shown in **Figure 2b** reveals the deposited components on the surface of the CF. Because rGO was synthesized from GO using a modified Hummer's method, the X-ray diffraction (XRD) pattern and Raman spectra for both materials were analyzed and compared to determine if the reduction from GO-to-rGO was successful. The XRD pattern of GO and rGO are depicted in **Figure 2c**, demonstrating its effective reduction of the rGO prior to its application to the CF. The interlayer spacing increased owing to the presence of O_2 molecule in GO powder which resulted in peak shifting to 11.5°. However, the elimination of oxygen functional groups after reducing GO to rGO decreases the space between two layers and shifts the peak to 24.7°. To observe the Raman spectra, we separately excited both the GO and rGO samples with a laser at a wavelength of 532 nm. As shown in **Figure 2c**, the D vibration band of GO and rGO can be seen at 1348.31 and 1353.20 cm^{-1}, respectively. This band is formed due to the A_{1g} symmetry.[54] The G vibration band, visible at 1594.19 cm^{-1} for GO and 1586.56 cm^{-1} for rGO, occurs due to the 1st order scattering of E_{2g} photons by sp^2 carbon.[54]

The G vibration band also benefits from the stretching C-C bond, which is present in all sp^2 carbon systems.[55] Since fewer oxygen-containing functional groups remained after GO was converted to rGO, the rGO stacked. Thus, the 2D band at 2892.88 cm^{-1} shifted upward and became wider following the reduction step.[56] GO has an I_D/I_G ratio of 0.96. After reduction, sp^2 carbon was restored, and the average size of the sp^2 domains shrank,

increasing the I_D/I_G ratio of rGO to 1.16.[57–60] More isolated graphene domains were found in rGO than in GO, and the removal of oxygen moieties from GO was also indicated by a rise in intensity in the D band.[61,62]
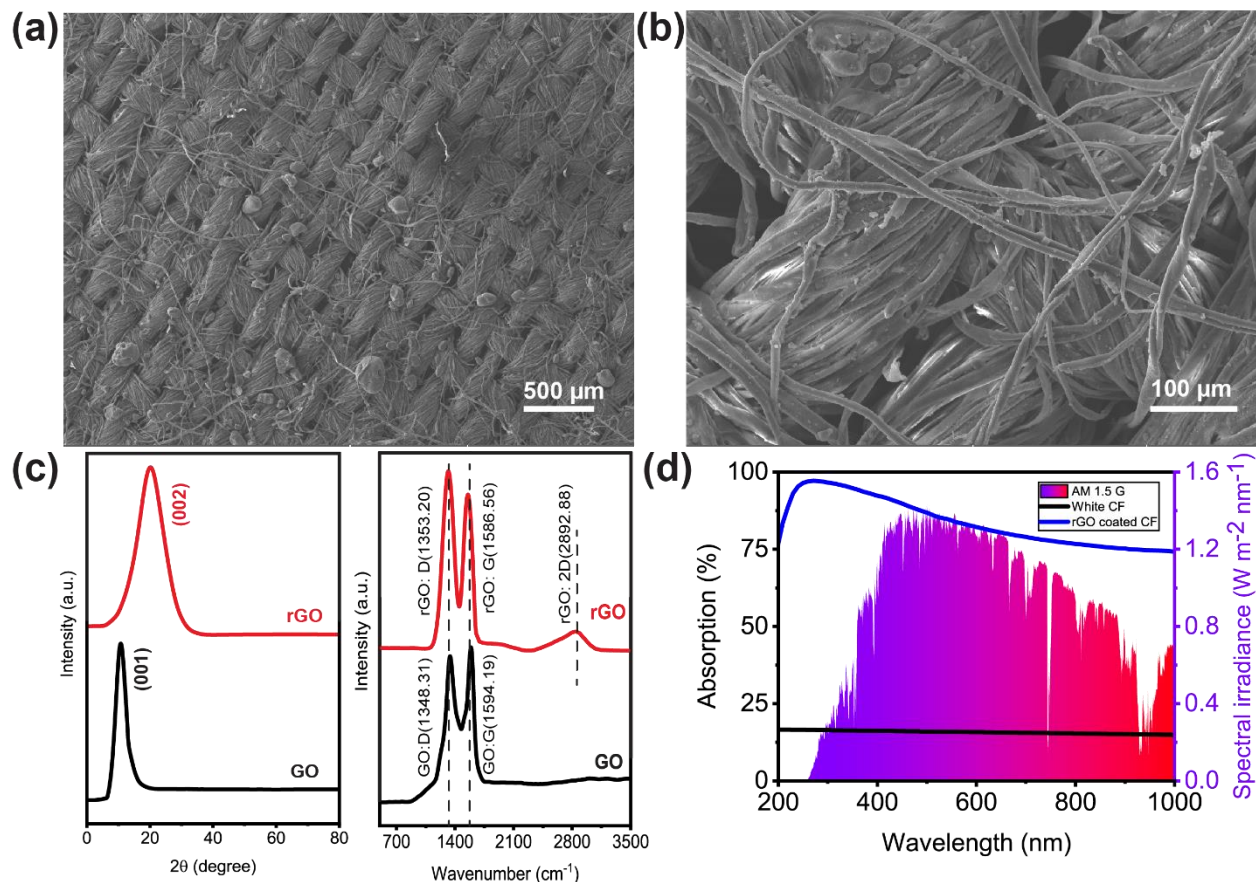
Figure 2. (a) – (b) Scanning electron microscopy (SEM) image of rGO coated CF at different magnification; (c) X-ray diffraction (XRD) pattern and Raman spectra (excited with 532 nm laser source) of GO and rGO before and after reduction; (d) UV-Vis absorption spectrum of cotton fabric and rGO coated cotton fabric.

The UV-Vis absorption spectra of the washed and dried CF, uncoated and rGO coated, can be seen in **Figure 2d**. The rGO coated CF showed wideband absorbance of about 82% weighted by the standard air mass 1.5 global solar spectrum across 200 – 1000 nm, while the uncoated CF showed only 19% absorbance over the same wavelength range. In a controlled laboratory context, the effectiveness of solar-powered steam generation is

assessed by monitoring the mass loss of water in response to changes in solar irradiance, temperature, and humidity (typically 20 ± 1 °C, 60 % relative humidity, RH). The experiments measured the loss in mass and the change in temperature.

Figure 3a shows that under 1 sun illumination (100 W/m^2 of irradiance), the mass loss of DI water without any solar evaporator was measured as 0.284 kg m^{-2} h^{-1}. For uncoated CF and the TEG module without a heat sink, the mass loss remained as low as 0.454 kg m^{-2} h^{-1}. The evaporation rate observed from rGO-coated CF without the TEG module measured at 0.431 kg m^{-2} h^{-1}. Notably, while the rGO coating enhanced solar absorption, the absence of the TEG module led to increased heat dissipation to the underlying bulk water, subsequently contributing to a reduction in solar evaporation. The rGO coating on the CF and TEG module enhanced the heat absorption, therefore, the mass loss increased to 1.308 kg m^{-2} h^{-1}. However, the attachment of the heat sink to the cold side of the TEG module provides superior separation between the evaporator surface and the bulk water, aiding the heat localization at the evaporator surface. As a result, the mass loss significantly increased to 1.741 kg m^{-2} h^{-1}. The remarkable absorption peak of rGO in the UV band significantly enhanced the evaporation performance. However, for the rGO-coated CF and TEG module with a heat sink, the water mass loss increases with the increase of incident solar irradiation. As can be seen in **Figure 3b**, the mass loss increased from 2.869 kg m^{-2} h^{-1} under 2 sun illumination to 4.455 kg m^{-2} h^{-1} under 3 sun illumination. Under 1 sun illumination, the rGO-coated CF and TEG module with heat sink evaporated water at a rate 6.78 times greater than the DI water evaporation rate (in the absence of any enhancements of the solar still) which was measured as just 1.385 kg m^{-2} h^{-1}. The evaporation efficiency was determined by taking into account the rate at which

water evaporates spontaneously in the dark. Note S2 of the ESI provides the equations for these calculations.
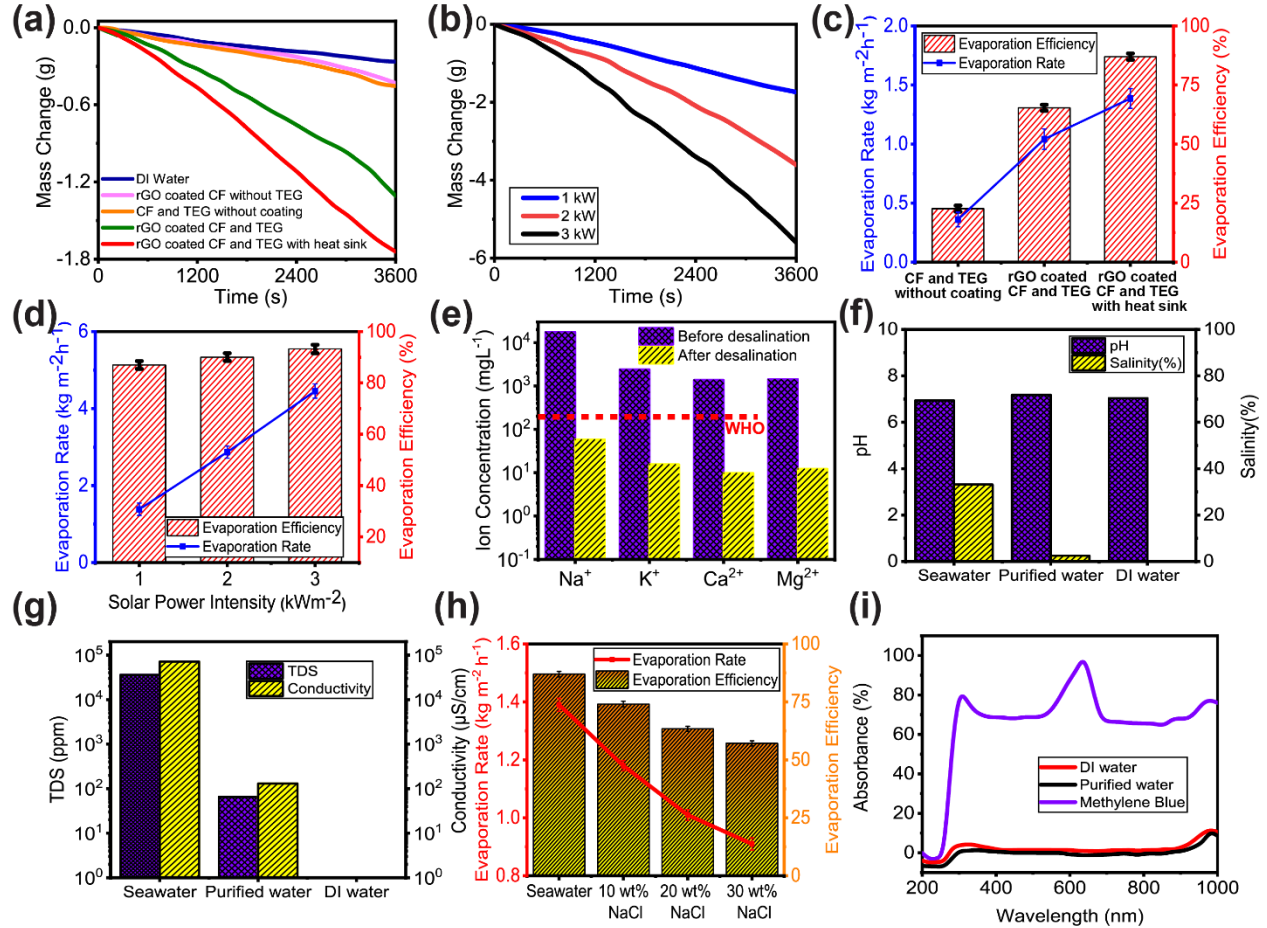
Figure 3. (a) The solar evaporation mass loss of uncoated CF and TEG structure, rGo-coated CF without TEF, rGO coated CF and TEG, and rGO-coated CF and TEG with heat sink under 1 sun illumination. (b) Mass loss of rGO-coated CF and TEG with heat sink structure under various solar irradiance. (c) Evaporation rate (line) and efficiency (bars) of the 3 different conditions tested and (d) rGO coated CF and TEG with heat sink structure under various solar irradiance. (e) The concentration of the four main salt ions (Na$^+$, K$^+$, Ca^{2+}, and Mg^{2+}) of actual seawater before and after desalination. (f) pH and salinity of the water before and after desalination compared to DI water, (g) Total dissolved solids (TDS), and conductivity of seawater, purified water, and DI water. (h) Evaporation rate (line) and efficiency (bars) of seawater and different salinity NaCl solutions. (f) The UV-Vis spectra of methylene blue before and after solar evaporation.

Under 1 sun irradiation, the rGO coated CF and TEG module with a heat sink was determined to have an evaporation efficiency of 86.98%. Whereas without a heat sink, evaporation efficiency drops to 65.34%. Therefore, the use of a heat sink has resulted in a notable improvement in the efficiency of evaporation. The TEG module and heat sink act as thermal insulation, while the CF's numerous microporous channels, hydrophilicity, and exceptional water transportability all contribute to the remarkable evaporation efficiency. **Figure 3d** shows that as solar irradiation rose, so did the evaporation rate and efficiency. While there was a linear rise in the rate of evaporation, there was some variation in the efficiency of that process. 15 TEG modules were coupled in a series-parallel arrangement, as indicated in the inset of **Figure 5**, and used in another set of solar evaporation experiments in a custom-made dome-shape structure as described in the material and methods section.

With just 1 sun irradiance, the dome-shaped construction, with the rGO coated CF and the TEG with heat sink which is shown in **Figure 5**, seawater evaporated effectively and condensed to create water droplets, producing thermal heat in the process. Evaporation efficiency was computed at 87.8%, which is slightly better than the efficiency attained in the small-scale laboratory setup (which was measured as 86.98%). The evaporation rate of seawater was recorded as $4.96 \ kg \ m^{-2} \ h^{-1}$. **Figure 3f-h** shows the results of utilizing the water quality tester EZ-9909SP to determine the concentration of total dissolved solids (TDS), conductivity, pH, and salinity in a specimen of the evaporated water which was collected as the condensed droplets ran off the dome surface. Inductively coupled plasma mass spectrometry (ICP-MS) was used to measure the ion concentrations (Na^+, K^+, Ca^{2+}, Mg^{2+}) in seawater and the desalinated water. As shown in **Figure 3e**, the ion

concentration of desalinated water is almost 3-4 orders of magnitude lower than that of seawater and is substantially below the World Health Organization's (WHO) salinity requirements for drinkable water. As presented in **Figure 3f-g**, seawater had a salinity of 33.2 % and a pH of 6.94, whereas the purified water had a salinity of 0.25% and a pH of 7.18. According to the World Health Organization, the optimal pH range for drinking water is between 6.5 and 8.5.[63] In terms of salinity and pH, purified water was essentially identical to DI water. The conductivity of seawater is 65 mS/cm and the TDS concentration is 35,975 ppm. However, the TDS and conductivity dropped to 65 ppm and 130 µS/cm, respectively, after being desalinated using the rGO coated CF. The World Health Organization (WHO)[64] states that a TDS of less than 600 mg/L(600 ppm) is acceptable for human consumption, and that a TDS of less than 300 mg/L (300 ppm) is excellent for human consumption of drinking water.[65]

Also, various wt% of brine water solutions were used to determine the evaporation rate and efficiency of the rGO coated CF. Evaporation efficiency reduced from 86.98% to 74.08% for a 10% brine water solution, as illustrated in **Figure 3h**. The evaporation rate and efficiency decreased as the wt% of NaCl in brine water solution rose. Despite this, no visible NaCl was observed on the surface of the rGO coated CF, showing its improved salt-rejecting ability. Salt deposition on the surface of the solar evaporator clogs the microporous channel of the evaporator, preventing the transfer of water molecules from the bulk water to the surface of the evaporator, hence diminishing its evaporation performance.[23,66] Therefore, it is vital to reject the salt accumulation on the evaporator's surface. The aligned, relatively large-diameter channels of CF enable crystallized salts to dissolve rapidly and be returned to the bulk water. All the foregoing

results indicate that the rGO coated CF has a high potential for use in practical solar water treatment to address freshwater scarcity challenges.

Furthermore, wastewater treatment experiments were carried out to assess the wastewater treatment performance of rGO coated CF. To replicate wastewater, a solution of methylene blue (MB) was selected as suggested by many literatures.[25,67,68] Purified water absorbance is comparable to DI water without the characteristic MB peaks displayed in **Figure 3i**, suggesting that the MB should be totally eliminated from the purified water, and remain in concentrated form in the residual brine.

Under 1 sun illumination, the output voltage of the TEG module was measured which is the result of the temperature difference between the hot and cool surfaces (the Seebeck effect). The hot surface temperature of the TEG module increases from 37.2 to 77.5 °C in only 15 mins, as shown in **Figure 4d.** A single TEG module has the capacity to constantly reproduce voltage of 395 mV, which is demonstrated by the cyclic on-off test as depicted in **Figure 4a**. The experimental set up to measure the single TEG module generated voltage is shown in **Figure 4b**. The TEG module's output voltage and the surface temperature's dynamic relationship over time are also shown in **Figure 4c**. The temperature of the top and bottom surface of the TEG module are recorded using a K-type thermocouple (model: CENTER 306). After 15 mins of exposure to 1 sun illumination, the temperature difference between the hot and cold sides of the TEG module reached 21 °C, while after 30 mins of exposure, the difference reached 56.6 °C. The bottom surface (cold side of the TEG) is kept below 45 °C by dissipating the heat using an aluminum heat sink and having the TEG completely submerged in water during the solar evaporation tests, even though both the top and bottom surfaces experience rapid

increases in temperature when the xenon lamp is switched on. After 90 minutes of xenon lamp operation, the produced voltage reaches a high of 780 mV, which is proportional to the increasing hot surface temperature.
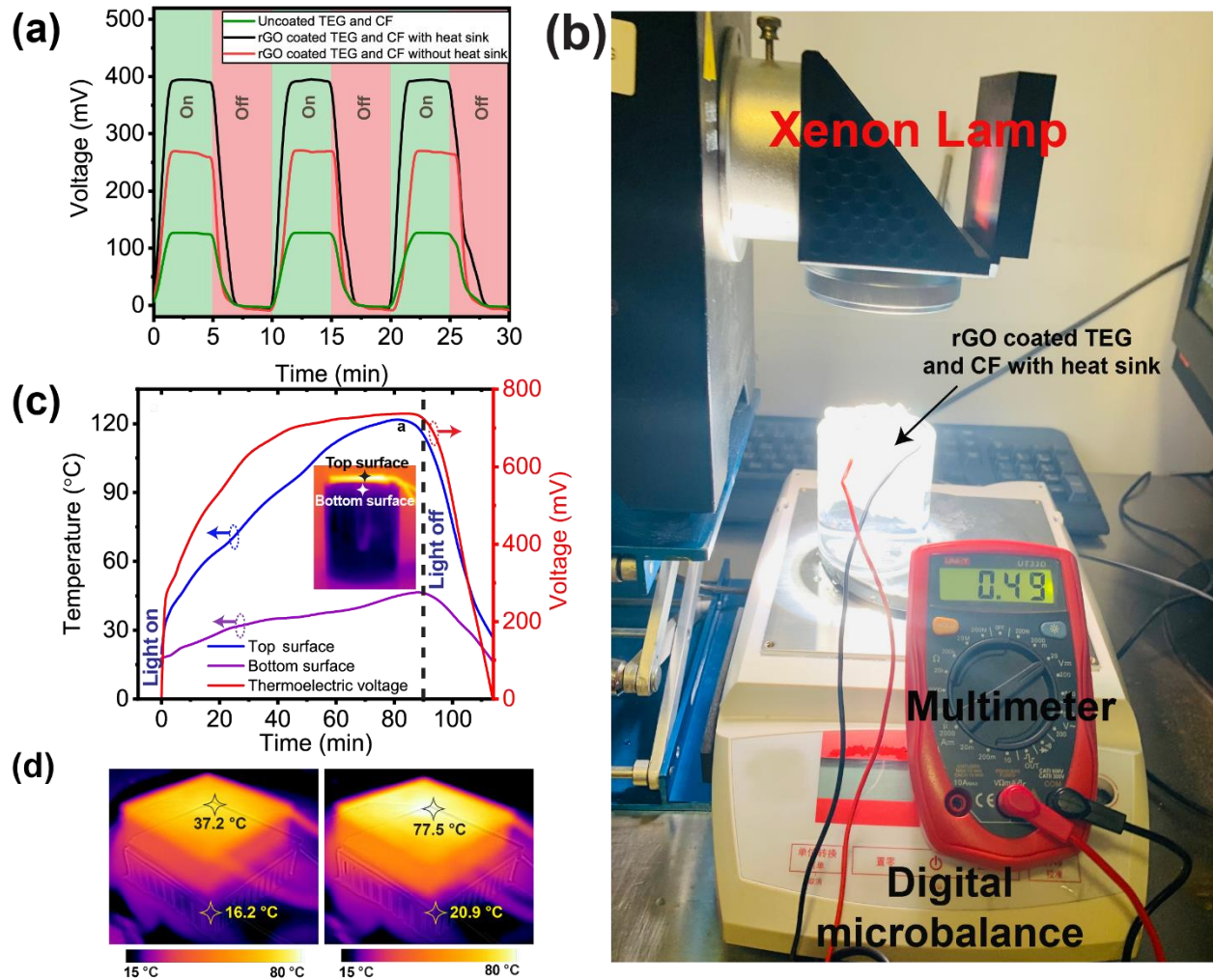
Figure 4. (a) Voltage generated by a single TEG module for different device structures (uncoated CF of rGO coated CF with / without heat sink) under 1 sun illumination. (b) The experimental setup for measuring mass loss due to solar evaporation and the voltage produced by a TEG module. (c) The voltage produced by the TEG module and its top and bottom surface temperatures when exposed to a 1 sun illumination. (d) Temperature difference between the top surface and bottom surface / heat sink after 15 mins (left) and after 30 mins (right) under 1 sun illumination.

Since the EPE foam around the setup serves to concentrate heat and prevent radiative heat loss, the top surface temperature, and generated voltage take around 20 minutes to

restore to zero when the xenon light is turned off (**Figure 4c**). Experiments were also conducted with and without an aluminum heat sink which helps to reduce the temperate of the cold side of the TEG by radiating heat. The results are shown in **Figure 4a** which provides a better understanding of the impact of using a heat sink. The TEG module with rGO coating but without a heat sink generated 260 mV of voltage in 5 minutes and after adding the heat sink to the cold side of the TEG module, the generated voltage in 5 minutes increased to 390 mV (i.e., a 50% improvement). By expanding the temperature gap between the hot and cold sides of the TEG module, the aluminum heat sink helps to boost the voltage output.

As long as two or more TEG modules are linked in series and parallel, enough voltage and current may be generated to run an electrical load like a tiny fan, LED lights, sensors, or other Internet of Things (IoT)-based devices. Our goal is to utilize the electricity generated by the TEG modules to power a water electrolysis system that will generate hydrogen gas on a small scale. To increase the voltage and current, 5 TEG modules were connected in series, and 3 sets of these were linked in parallel (for a total of 15 TEG modules). All 15 TEG modules were housed in a single piece of EPE foam with a 9 cm radius cut out of it, coupled in a series-parallel arrangement, as illustrated in the inset of **Figure 5**. rGO coating was applied to the hot surfaces of all TEG modules. As described in section 2, 15 individual CF with rGO coating were made to encase the TEG modules and to slip into the space between the TEG modules and the EPE foam. As can be seen in **Figure 5**, this new structure was placed into a tailor-made dome shape ISSG structure to establish a unique water-energy nexus in which solar evaporation and TEG-based power electricity production experiments was carried out. Under the influence of solar

irradiation or a xenon lamp, water vapor condenses at the inner side of the dome-shaped structure, forming water droplets as it radiates heat into the surroundings. The dome-shaped structure is split into two chambers as described in section 2. Because the outer chamber's base is sloped toward the drain-out channel, water can be collected with relative ease from the bottom of the dome structure (labeled outlet in **Figure 5**). During the solar evaporation process, the inner chamber must be kept full of seawater in part to cool the lower surface but also as the source of water for evaporation, thus a second inflow pipe is attached to provide seawater.
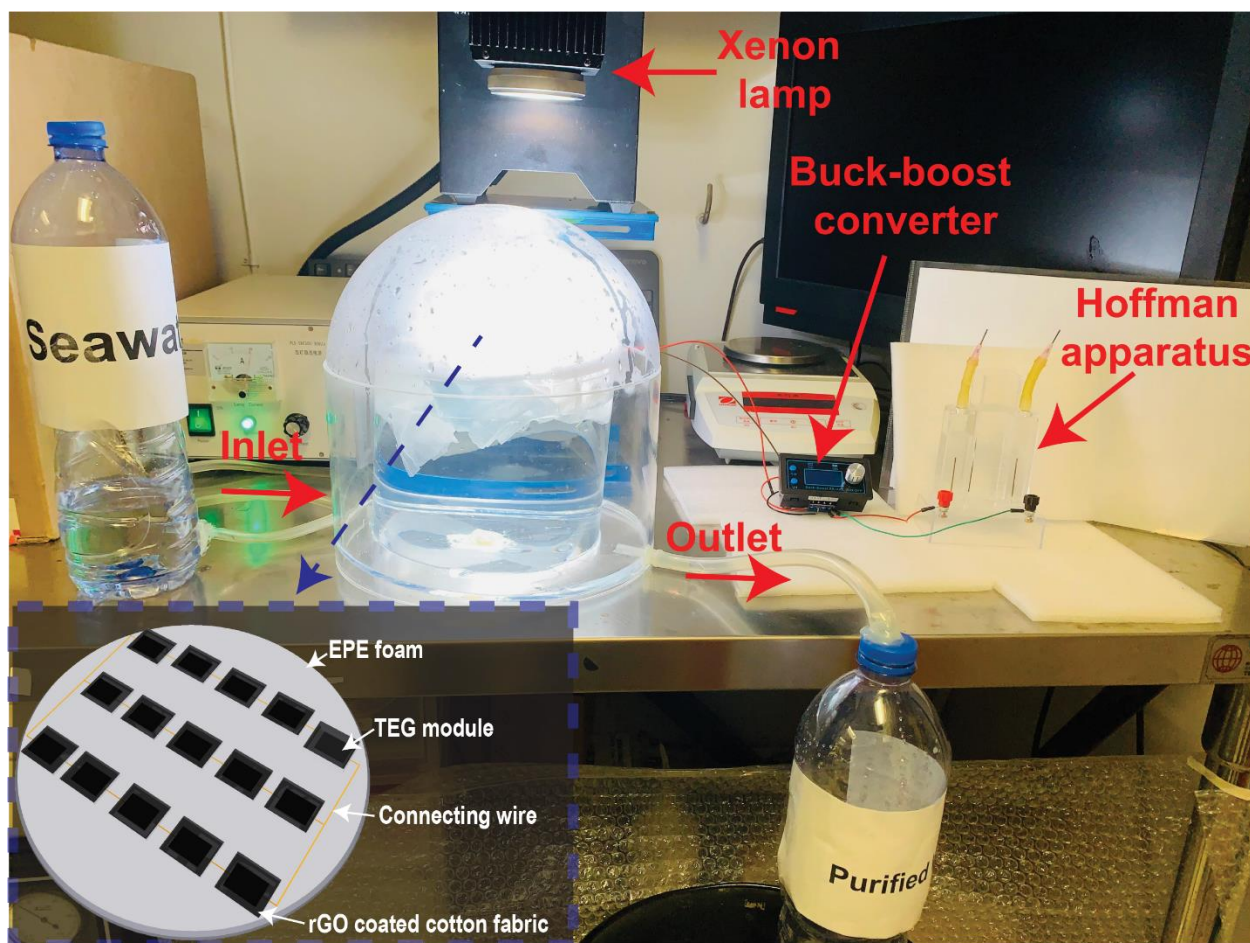
Figure 5. Experimental setup of seawater evaporation, electricity generation using TEG module, and seawater electrolysis with generated electricity to produce hydrogen. The inset shows the series-parallel connection of the TEG modules.

During the experiments, the generated voltage by the 15 TEG modules, connected in a series-parallel combination, was measured. The open circuit voltage of the series-parallel arrangement was 3.72 V and the short-circuit current was 449.55 mA under 1 sun illumination (**Figure 6a**), whereas the corresponding values for a single TEG cell were 0.724 V and 150.85 mA, respectively.
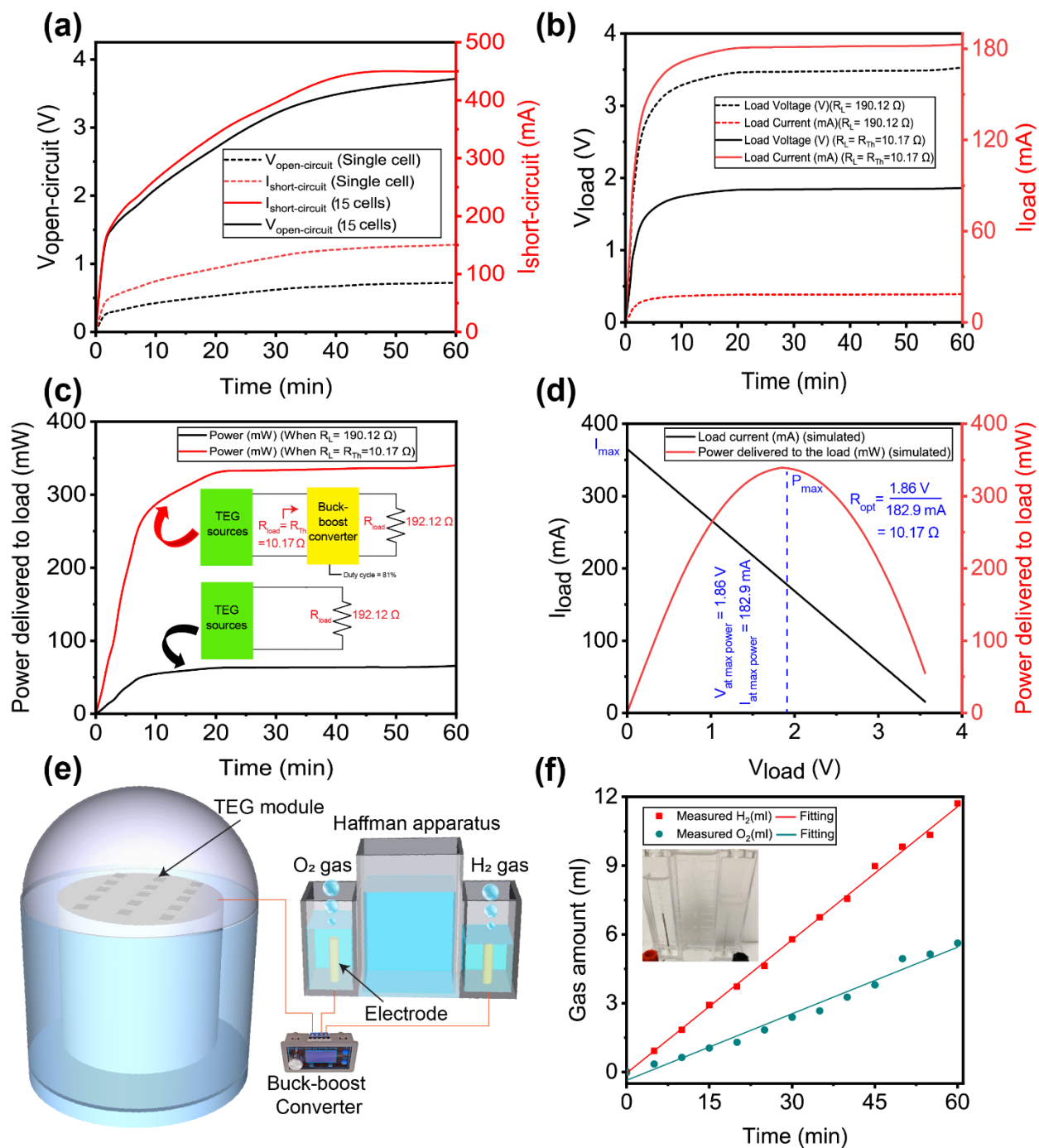
The open-circuit voltage and short-circuit current obtained under 1 sun illumination in our approach significantly surpass those achieved by other recent methods used for electricity production. A comprehensive performance comparison, as presented in **Table 1**, highlights the substantial superiority of our proposed method in harnessing photothermal energy for electricity generation.

Table 1. Performance comparison of electricity generation from photothermal energy

Method used to produce electricity	Open circuit voltage (mV) under 1 sun	Short-circuit current (mA) under 1 sun	Theoretical maximum Power (mW) under 1 sun	Ref.
MoS_{2-x} NSAs/TE module	98.2	13.5	1.33	[69]
CNT/TEG module	0.5	0.055	0.0007	[70]
CTGS/paper-TEG module	185.95	0.957	0.178	[71]
Cu Nps@Zn foil/TEG module	200	1.3	0.26	[72]
rGO-CF/TEG module	724	150.85	109.22	This work

As illustrated in **Figure 4(b)**, the voltage of a single TEG module was measured in an open environment. As a consequence, the radiative heat loss from the hot side of the TEG module is greater. However, after connecting 15 TEG modules in a series-parallel configuration, the experiment was carried out within the closed dome-shaped construction depicted in **Figure 5**. Because of the closed structure, heat energy was retained within,

raising the hot-side temperature of the TEG module even higher. Because the cold side was connected to a heat sink and immersed in water, a greater differential temperature was formed, resulting in increased voltage production by the TEG modules. As a result, the voltage generated by the 15 TEG modules linked in series parallel is greater than the peak voltage of the sum of a single TEG. The heat-to-electricity conversion efficiency of the TEG module was determined to be 7.3%; the detailed calculation is provided in note S5 of the ESI. This converted energy would have been lost from the system as radiated heat if the TEG modules had not been used. As a result, it can be claimed that adding the TEG module yielded a 7.3% overall improvement in system efficiency.

Figure 6. (a) The open-circuit voltage and short-circuit current curves for single cell and 15 cells of TEG modules; (b) the voltage and current and (c) power with connected Cu electrode and with Thevenin equivalent resistance (d) simulated load current and power delivered to the load; (e) graphical illustration of the practical setup; (f) generated H_2 and O_2 gas during electrolysis process (inset: Huffman apparatus).

The brine electrolysis experiment was conducted utilizing a customized Hoffman setup, as shown in **Figure S4** of **ESI**. For the electrolysis of the brine water, copper electrodes were utilized since they work better than graphite electrodes.[73] The Hoffman apparatus's Cu electrode was wired to the TEG modules' output terminal. As can be seen in **Figure 6b**, the measured resistance of the copper electrode submerged into the brine was 190.12 Ω, which consumes 178.1 mA of current keeping the terminal voltage at less than 0.5 V. However, if the value of the connected resistance had been 10.17 Ω (obtained from the Thevenin equivalent resistance calculation, details are provided in **note S6** of **ESI)**, it would have consumed 182.6 mA of current at a terminal voltage of 3.49 V. Therefore, maximum power extraction from the system for this particular configuration will only be possible if the value of the connected electrical resistance is close to 10.17 Ω.

To tune the resistance of the connected Cu electrode to this optimum value, we designed a buck-boost converter, as shown in **Figures 5 and 6e**, to guarantee that the maximum possible power from the TEG modules' output can be provided to the electrolysis equipment. To balance the resistance of the Cu electrode, which was submerged into the brine, with the Thevenin equivalent resistance (=10.17 Ω), the duty cycle of the converted buck-boost was determined to be 81%. Note S4 of the ESI contains the equations used for these calculations. As can be seen in **Figure 6b**, the TEG modules and the Cu electrode of the Hoffman apparatus are connected to a buck-boost converter operating at 81% duty cycle, which provides maximum power extraction by delivering 182 mA at a terminal voltage of 3.49 V.

According to **Figure 6c**, introducing a buck-boost converter increased the power delivered to the Cu electrode of the electrolysis equipment from 64 mW to 336.17 mW.

To verify that the extracted 336.17 mW is the maximum power that can be obtained from the TEG modules for this particular series-parallel configuration, a MATLAB Simulink was carried out, as shown in **Figure S5** (ESI). The simulation varied the connected electrical resistance and simulated the output current, voltage, and power. After plotting the simulated values, as shown in **Figure 6c**, it can be seen that 336.17 mW power is the maximum possible output power and the corresponding electrical resistance for this maximum power is 10.17 Ω which is exactly the same as the Thevenin equivalent resistance which was found after connecting the buck-boost converter operating at 81% duty cycle.

As mentioned before, the Cu electrodes of the Hoffman apparatus were connected to the output terminal of the TEG modules. On the cathode and anode, hydrogen and oxygen evolved respectively. **Note S7 of the ESI** provides the chemical reaction equations and electrode potentials. Molecular H_2 and O_2 are generated by an electrochemical reaction on the electrode surface during electrolysis and forms foam bubbles. The supporting movie shows persistent bubbling throughout the experiment. Putting a lit splint near the gas collection tube allows it to explode, proving hydrogen gas generation. A lighting splint re-ignites when placed in an oxygen gas collecting tube, confirming its presence. **Figure 6f** indicates that the measured gas produces 11.57 mL/h of hydrogen and 5.63 mL/h of oxygen. The suggested rGO-coated CF functions as an efficient solar absorber that supplies freshwater at an efficiency of 86.98%, while the remaining solar heat is utilized to produce electricity from TEG modules, which can be used to electrolyze brine to produce hydrogen gas. Electrolysis is a low-cost method for extracting water from brine because the salt components are deposited at the electrodes and at the bottom of the

electrolysis unit while the water is converted into hydrogen and oxygen gas. The deposited salt may be recovered and used in various applications. Thereby, the proposed system demonstrated its potential for remediating desalination waste in a cost-effective manner.

4. CONCLUSION

In summary, the rGO-coated cotton fabric (CF) solar interfacial steam generation system presented herein has been demonstrated to produce desalinated water with an evaporation efficiency of 86.98%. The proposed ISSG also has salt-rejection capabilities owing to the aligned and relatively large-diameter channels of the CF, preventing pore blockage, and thereby ensuring continued efficiency. The system also incorporated the use of TEG modules to produce electricity from the photothermal heat. 15 TEG modules are cascaded to produce 339.26 mW of electricity which can run a brine water electrolysis system to produce hydrogen gas at a rate of 0.52 mmol/h. The use of photothermal heat to produce electricity in parallel with solar desalination increases the overall system efficiency by 7.3%. The power is then utilized to electrolyze the brine, converting the brine into hydrogen gas at a rate of 0.52 mmol/h, which might solve the disposal problem associated with brine from ISSG systems. Hydrogen gas can be stored in cylinders for later use in fuel cells, for ammonia synthesis or methanation, for example. The potential to replace environmentally damaging battery packs with hydrogen gas storage for renewable energy storage systems is demonstrated.

Conflicts of interest

There is no conflict to declare.

Acknowledgments

References

[1]   V.P. Wright, World Energy Outlook., (1986) 23–28.

[2]   M. Amjad, G. Raza, Y. Xin, S. Pervaiz, J. Xu, X. Du, D. Wen, Volumetric solar heating and steam generation via gold nanofluids, Appl Energy. 206 (2017) 393–400. https://doi.org/10.1016/j.apenergy.2017.08.144.

[3]   K.-K. Liu, Q. Jiang, S. Tadepalli, R. Raliya, P. Biswas, R.R. Naik, S. Singamaneni, Wood–Graphene Oxide Composite for Highly Efficient Solar Steam Generation and Desalination, ACS Appl Mater Interfaces. 9 (2017) 7675–7681. https://doi.org/10.1021/acsami.7b01307.

[4]   Y. Wang, X. Wu, T. Gao, Y. Lu, X. Yang, G.Y. Chen, G. Owens, H. Xu, Same materials, bigger output: A reversibly transformable 2D–3D photothermal evaporator for highly efficient solar steam generation, Nano Energy. 79 (2021). https://doi.org/10.1016/j.nanoen.2020.105477.

[5]   E.-D. Miao, M.-Q. Ye, C.-L. Guo, L. Liang, Q. Liu, Z.-H. Rao, Enhanced solar steam generation using carbon nanotube membrane distillation device with heat localization, Appl Therm Eng. 149 (2019) 1255–1264. https://doi.org/10.1016/j.applthermaleng.2018.12.123.

[6]   T. Chen, Z. Wu, Z. Liu, J.T. Aladejana, X. (Alice) Wang, M. Niu, Q. Wei, Y. Xie, Hierarchical Porous Aluminophosphate-Treated Wood for High-Efficiency Solar Steam Generation, ACS Appl Mater Interfaces. 12 (2020) 19511–19518. https://doi.org/10.1021/acsami.0c01815.

[7]   Md.N.A.S. Ivan, A.M. Saleque, S. Ahmed, P.K. Cheng, J. Qiao, T.I. Alam, Y.H. Tsang, Waste Egg Tray and Toner-Derived Highly Efficient 3D Solar Evaporator for Freshwater Generation, ACS Appl Mater Interfaces. 14 (2022) 7936–7948. https://doi.org/10.1021/acsami.1c22215.

[8] A.M. Saleque, S. Ahmed, Md.N.A.S. Ivan, M.I. Hossain, W. Qarony, P.K. Cheng, J. Qiao, Z.L. Guo, L. Zeng, Y.H. Tsang, High-temperature solar steam generation by MWCNT-HfTe2 van der Waals heterostructure for low-cost sterilization, Nano Energy. 94 (2022) 106916. https://doi.org/10.1016/j.nanoen.2022.106916.

[9] Z. Guo, Z. Chen, Z. Shi, J. Qian, J. Li, T. Mei, J. Wang, X. Wang, P. Shen, Stable metallic 1T phase engineering of molybdenum disulfide for enhanced solar vapor generation, Solar Energy Materials and Solar Cells. (2020). https://doi.org/10.1016/j.solmat.2019.110227.

[10] L. Zhang, L. Mu, Q. Zhou, X. Hu, Solar-assisted fabrication of dimpled 2H-MoS2 membrane for highly efficient water desalination, Water Res. (2020). https://doi.org/10.1016/j.watres.2019.115367.

[11] N. Wei, Z. Li, Q. Li, E. Yang, R. Xu, X. Song, J. Sun, C. Dou, J. Tian, H. Cui, Scalable and low-cost fabrication of hydrophobic PVDF/WS2 porous membrane for highly efficient solar steam generation, J Colloid Interface Sci. 588 (2021) 369–377. https://doi.org/10.1016/j.jcis.2020.12.084.

[12] A.M. Saleque, S. Ahmed, Md.N.A.S. Ivan, M.I. Hossain, W. Qarony, Y.H. Tsang, Localized surface plasmon resonance induced temperature enhancement by MWCNT-HfTe2 van der Waals heterostructure, in: A. Majumdar, C.M. Torres, H. Deng (Eds.), 2D Photonic Materials and Devices V, SPIE, 2022: p. 39. https://doi.org/10.1117/12.2623411.

[13] K. Li, T. Chang, Z. Li, H. Yang, F. Fu, T. Li, J.S. Ho, P. Chen, Light-to-Heat Conversion: Biomimetic MXene Textures with Enhanced Light-to-Heat Conversion for Solar Steam Generation and Wearable Thermal Management (Adv. Energy Mater. 34/2019), Adv Energy Mater. 9 (2019) 1970141. https://doi.org/10.1002/aenm.201970141.

[14] X. Zhao, L.M. Peng, C.Y. Tang, J.H. Pu, X.J. Zha, K. Ke, R.Y. Bao, M.B. Yang, W. Yang, All-weather-available, continuous steam generation based on the synergistic photo-thermal and electro-thermal conversion by MXene-based aerogels, Mater Horiz. 7 (2020) 855–865. https://doi.org/10.1039/c9mh01443h.

[15] X. Li, X. Li, H. Li, Y. Zhao, W. Li, S. Yan, Z. Yu, 2D Ferrous Ion-Crosslinked Ti 3 C 2 T x MXene Aerogel Evaporators for Efficient Solar Steam Generation, Adv Sustain Syst. 5 (2021) 2100263. https://doi.org/10.1002/adsu.202100263.

[16] K. Li, T. Chang, Z. Li, H. Yang, F. Fu, T. Li, J.S. Ho, P. Chen, Biomimetic MXene Textures with Enhanced Light-to-Heat Conversion for Solar Steam Generation and Wearable Thermal Management, Adv Energy Mater. 9 (2019) 1901687. https://doi.org/10.1002/aenm.201901687.

[17] A.K. Thakur, R. Sathyamurthy, R. Saidur, R. Velraj, I. Lynch, N. Aslfattahi, Exploring the potential of MXene-based advanced solar-absorber in improving the performance and efficiency of a solar-desalination unit for brackish water purification, Desalination. 526 (2022) 115521. https://doi.org/10.1016/j.desal.2021.115521.

[18] X. Fan, Y. Yang, X. Shi, Y. Liu, H. Li, J. Liang, Y. Chen, A MXene-Based Hierarchical Design Enabling Highly Efficient and Stable Solar-Water Desalination with Good Salt

Resistance, Adv Funct Mater. 30 (2020) 2007110.
https://doi.org/10.1002/adfm.202007110.

[19]   P. Sun, W. Wang, W. Zhang, S. Zhang, J. Gu, L. Yang, D. Pantelić, B. Jelenković, D.
Zhang, 3D Interconnected Gyroid Au–CuS Materials for Efficient Solar Steam
Generation, ACS Appl Mater Interfaces. 12 (2020) 34837–34847.
https://doi.org/10.1021/acsami.0c06701.

[20]   H. Liu, C. Chen, H. Wen, R. Guo, N.A. Williams, B. Wang, F. Chen, L. Hu, Narrow
bandgap semiconductor decorated wood membrane for high-efficiency solar-assisted
water purification, J Mater Chem A Mater. 6 (2018) 18839–18846.
https://doi.org/10.1039/C8TA05924A.

[21]   K.W. Tan, C.M. Yap, Z. Zheng, C.Y. Haw, P.S. Khiew, W.S. Chiu, State-of-the-Art
Advances, Development, and Challenges of Metal Oxide Semiconductor Nanomaterials
for Photothermal Solar Steam Generation, Adv Sustain Syst. (2022) 2100416.
https://doi.org/10.1002/adsu.202100416.

[22]   A.M. Saleque, S. Ma, S. Ahmed, M.I. Hossain, W. Qarony, Y.H. Tsang, Solar Driven
Interfacial Steam Generation Derived from Biodegradable Luffa Sponge, Adv Sustain
Syst. 5 (2021) 2000291. https://doi.org/10.1002/adsu.202000291.

[23]   Y. Kuang, C. Chen, S. He, E.M. Hitz, Y. Wang, W. Gan, R. Mi, L. Hu, A High-
Performance Self-Regenerating Solar Evaporator for Continuous Water Desalination,
Advanced Materials. 31 (2019) 1900498. https://doi.org/10.1002/adma.201900498.

[24]   C. Sheng, N. Yang, Y. Yan, X. Shen, C. Jin, Z. Wang, Q. Sun, Bamboo decorated with
plasmonic nanoparticles for efficient solar steam generation, Appl Therm Eng. 167 (2020)
114712. https://doi.org/10.1016/j.applthermaleng.2019.114712.

[25]   S. Ma, C.P. Chiu, Y. Zhu, C.Y. Tang, H. Long, W. Qarony, X. Zhao, X. Zhang, W.H. Lo,
Y.H. Tsang, Recycled waste black polyurethane sponges for solar vapor generation and
distillation, Appl Energy. 206 (2017) 63–69.
https://doi.org/10.1016/j.apenergy.2017.08.169.

[26]   Q. Fang, T. Li, H. Lin, R. Jiang, F. Liu, Highly Efficient Solar Steam Generation from
Activated Carbon Fiber Cloth with Matching Water Supply and Durable Fouling
Resistance, ACS Appl Energy Mater. 2 (2019) 4354–4361.
https://doi.org/10.1021/acsaem.9b00562.

[27]   Y. Zhou, T. Ding, M. Gao, K.H. Chan, Y. Cheng, J. He, G.W. Ho, Controlled
heterogeneous water distribution and evaporation towards enhanced photothermal water-
electricity-hydrogen production, Nano Energy. 77 (2020) 105102.
https://doi.org/10.1016/j.nanoen.2020.105102.

[28]   F. Gong, W. Wang, H. Li, D. (David) Xia, Q. Dai, X. Wu, M. Wang, J. Li, D. V.
Papavassiliou, R. Xiao, Solid waste and graphite derived solar steam generator for
highly-efficient and cost-effective water purification, Appl Energy. 261 (2020) 114410.
https://doi.org/10.1016/j.apenergy.2019.114410.

[29] A.M. Saleque, N. Nowshin, Md.N.A.S. Ivan, S. Ahmed, Y.H. Tsang, Natural Porous Materials for Interfacial Solar Steam Generation toward Clean Water Production, Solar RRL. (2022) 2100986. https://doi.org/10.1002/solr.202100986.

[30] X. Hu, W. Xu, L. Zhou, Y. Tan, Y. Wang, S. Zhu, J. Zhu, Tailoring Graphene Oxide-Based Aerogels for Efficient Solar Steam Generation under One Sun, Advanced Materials. 29 (2017) 1604031. https://doi.org/10.1002/adma.201604031.

[31] T. Chen, S. Wang, Z. Wu, X. (Alice) Wang, J. Peng, B. Wu, J. Cui, X. Fang, Y. Xie, N. Zheng, A cake making strategy to prepare reduced graphene oxide wrapped plant fiber sponges for high-efficiency solar steam generation, J Mater Chem A Mater. 6 (2018) 14571–14576. https://doi.org/10.1039/C8TA04420A.

[32] H.M. Wilson, S. Rahman A.R., A.E. Parab, N. Jha, Ultra-low cost cotton based solar evaporation device for seawater desalination and waste water purification to produce drinkable water, Desalination. 456 (2019) 85–96. https://doi.org/10.1016/j.desal.2019.01.017.

[33] Z. Guo, G. Wang, X. Ming, T. Mei, J. Wang, J. Li, J. Qian, X. Wang, PEGylated Self-Growth MoS 2 on a Cotton Cloth Substrate for High-Efficiency Solar Energy Utilization, ACS Appl Mater Interfaces. 10 (2018) 24583–24589. https://doi.org/10.1021/acsami.8b08019.

[34] J. Zhao, X. Wu, H. Yu, Y. Wang, P. Wu, X. Yang, D. Chu, G. Owens, H. Xu, Regenerable aerogel-based thermogalvanic cells for efficient low-grade heat harvesting from solar radiation and interfacial solar evaporation systems, EcoMat. 5 (2023). https://doi.org/10.1002/eom2.12302.

[35] H. Yu, D. Wang, H. Jin, P. Wu, X. Wu, D. Chu, Y. Lu, X. Yang, H. Xu, 2D MoN $_{1.2}$ -rGO Stacked Heterostructures Enabled Water State Modification for Highly Efficient Interfacial Solar Evaporation, Adv Funct Mater. 33 (2023). https://doi.org/10.1002/adfm.202214828.

[36] H. Wang, W. Xie, B. Yu, B. Qi, R. Liu, X. Zhuang, S. Liu, P. Liu, J. Duan, J. Zhou, Simultaneous Solar Steam and Electricity Generation from Synergistic Salinity-Temperature Gradient, Adv Energy Mater. 11 (2021) 2100481. https://doi.org/10.1002/aenm.202100481.

[37] G. Ni, G. Li, S. V. Boriskina, H. Li, W. Yang, T. Zhang, G. Chen, Steam generation under one sun enabled by a floating structure with thermal concentration, Nat Energy. 1 (2016) 16126. https://doi.org/10.1038/nenergy.2016.126.

[38] M. Zhu, Y. Li, G. Chen, F. Jiang, Z. Yang, X. Luo, Y. Wang, S.D. Lacey, J. Dai, C. Wang, C. Jia, J. Wan, Y. Yao, A. Gong, B. Yang, Z. Yu, S. Das, L. Hu, Tree-Inspired Design for High-Efficiency Water Extraction, Advanced Materials. 29 (2017) 1704107. https://doi.org/10.1002/adma.201704107.

[39] P. Xiao, J. He, F. Ni, C. Zhang, Y. Liang, W. Zhou, J. Gu, J. Xia, S.-W. Kuo, T. Chen, Exploring interface confined water flow and evaporation enables solar-thermal-electro integration towards clean water and electricity harvest via asymmetric functionalization strategy, Nano Energy. 68 (2020) 104385. https://doi.org/10.1016/j.nanoen.2019.104385.

[40] Y. Xu, S. Dong, Y. Sheng, C. Liu, F. Xing, Y. Di, Z. Gan, Highly efficient solar driven cogeneration of freshwater and electricity, J Mater Chem A Mater. 11 (2023) 1866–1876. https://doi.org/10.1039/D2TA08590A.

[41] Z. Sun, W. Zhang, J. Guo, J. Song, X. Deng, Is Heat Really Beneficial to Water Evaporation-Driven Electricity?, J Phys Chem Lett. 12 (2021) 12370–12375. https://doi.org/10.1021/acs.jpclett.1c03718.

[42] A. Panagopoulos, K.-J. Haralambous, M. Loizidou, Desalination brine disposal methods and treatment technologies - A review, Science of The Total Environment. 693 (2019) 133545. https://doi.org/10.1016/j.scitotenv.2019.07.351.

[43] M.N. Soliman, F.Z. Guen, S.A. Ahmed, H. Saleem, M.J. Khalil, S.J. Zaidi, Energy consumption and environmental impact assessment of desalination plants and brine disposal strategies, Process Safety and Environmental Protection. 147 (2021) 589–608. https://doi.org/10.1016/j.psep.2020.12.038.

[44] A.M.O. Mohamed, M. Maraqa, J. Al Handhaly, Impact of land disposal of reject brine from desalination plants on soil and groundwater, Desalination. 182 (2005) 411–433. https://doi.org/10.1016/j.desal.2005.02.035.

[45] M. Yue, H. Lambert, E. Pahon, R. Roche, S. Jemei, D. Hissel, Hydrogen energy systems: A critical review of technologies, applications, trends and challenges, Renewable and Sustainable Energy Reviews. 146 (2021) 111180. https://doi.org/10.1016/j.rser.2021.111180.

[46] P. Puranen, A. Kosonen, J. Ahola, Technical feasibility evaluation of a solar PV based off-grid domestic energy system with battery and hydrogen energy storage in northern climates, Solar Energy. 213 (2021) 246–259. https://doi.org/10.1016/j.solener.2020.10.089.

[47] W. Bentzen, J. J. and Joergensen, P.S. and Zhang, Wei and Reissner, R. and Schiller, Günter and Guelzow, E. and van Craenendonck, B. and Vaes, J. and Alvarez Gallego, Y. and Doyen, Degradation of alkaline electrolyser electrodes, 3rd INTERNATIONAL WORKSHOP ON DEGRADATION ISSUES OF FUEL CELLS and ELECTROLYSERS. (2015).

[48] W. Mrozik, M.A. Rajaeifar, O. Heidrich, P. Christensen, Environmental impacts, pollution sources and pathways of spent lithium-ion batteries, Energy Environ Sci. 14 (2021) 6099–6121. https://doi.org/10.1039/D1EE00691F.

[49] O.J. Guerra, J. Eichman, J. Kurtz, B.-M. Hodge, Cost Competitiveness of Electrolytic Hydrogen, Joule. 3 (2019) 2425–2443. https://doi.org/10.1016/j.joule.2019.07.006.

[50] J. Yates, R. Daiyan, R. Patterson, R. Egan, R. Amal, A. Ho-Baille, N.L. Chang, Techno-economic Analysis of Hydrogen Electrolysis from Off-Grid Stand-Alone Photovoltaics Incorporating Uncertainty Analysis, Cell Rep Phys Sci. 1 (2020) 100209. https://doi.org/10.1016/j.xcrp.2020.100209.

[51] E. Rivard, M. Trudeau, K. Zaghib, Hydrogen Storage for Mobility: A Review, Materials. 12 (2019) 1973. https://doi.org/10.3390/ma12121973.

[52] L. Van Hoecke, L. Laffineur, R. Campe, P. Perreault, S.W. Verbruggen, S. Lenaerts, Challenges in the use of hydrogen for maritime applications, Energy Environ Sci. 14 (2021) 815–843. https://doi.org/10.1039/D0EE01545H.

[53] S. Thakur, N. Karak, Green reduction of graphene oxide by aqueous phytoextracts, Carbon N Y. 50 (2012) 5331–5339. https://doi.org/10.1016/j.carbon.2012.07.023.

[54] M.S. Dresselhaus, A. Jorio, M. Hofmann, G. Dresselhaus, R. Saito, Perspectives on Carbon Nanotubes and Graphene Raman Spectroscopy, Nano Lett. 10 (2010) 751–758. https://doi.org/10.1021/nl904286r.

[55] S. Thakur, N. Karak, Green reduction of graphene oxide by aqueous phytoextracts, Carbon N Y. 50 (2012) 5331–5339. https://doi.org/10.1016/j.carbon.2012.07.023.

[56] M.J.-Y. Tai, W.-W. Liu, C.-S. Khe, N.M.S. Hidayah, Y.-P. Teoh, C.H. Voon, H.C. Lee, P.Y.P. Adelyn, Green synthesis of reduced graphene oxide using green tea extract, in: 2018: p. 020032. https://doi.org/10.1063/1.5080845.

[57] P. Cui, J. Lee, E. Hwang, H. Lee, One-pot reduction of graphene oxide at subzero temperatures, Chemical Communications. 47 (2011) 12370. https://doi.org/10.1039/c1cc15569e.

[58] F. Tuinstra, J.L. Koenig, Raman Spectrum of Graphite, J Chem Phys. 53 (1970) 1126–1130. https://doi.org/10.1063/1.1674108.

[59] S. Stankovich, R.D. Piner, S.T. Nguyen, R.S. Ruoff, Synthesis and exfoliation of isocyanate-treated graphene oxide nanoplatelets, Carbon N Y. 44 (2006) 3342–3347. https://doi.org/10.1016/j.carbon.2006.06.004.

[60] Y. Wang, Z. Shi, J. Yin, Facile Synthesis of Soluble Graphene via a Green Reduction of Graphene Oxide in Tea Solution and Its Biocomposites, ACS Appl Mater Interfaces. 3 (2011) 1127–1133. https://doi.org/10.1021/am1012613.

[61] P. Cui, J. Lee, E. Hwang, H. Lee, One-pot reduction of graphene oxide at subzero temperatures, Chemical Communications. 47 (2011) 12370. https://doi.org/10.1039/c1cc15569e.

[62] D. Quality, pH in Drinking-water Revised background document for development of, Guidelines for Drinking-Water Quality. (2007).

[63] F. Addendum, T.O. Third, Guidelines for Drinking-water Quality, World Health Organization, Guidelines for Drinking-Water Quality. 1 (n.d.).

[64] D. Quality, pH in Drinking-water Revised background document for development of, Guidelines for Drinking-Water Quality. (2007).

[65] F. Wang, D. Wei, Y. Li, T. Chen, P. Mu, H. Sun, Z. Zhu, W. Liang, A. Li, Chitosan/reduced graphene oxide-modified spacer fabric as a salt-resistant solar absorber for efficient solar steam generation, J Mater Chem A Mater. 7 (2019) 18311–18317. https://doi.org/10.1039/C9TA05859A.

[66]   X. Zhao, X.J. Zha, J.H. Pu, L. Bai, R.Y. Bao, Z.Y. Liu, M.B. Yang, W. Yang, Macroporous three-dimensional MXene architectures for highly efficient solar steam generation, J Mater Chem A Mater. 7 (2019) 10446–10455. https://doi.org/10.1039/c9ta00176j.

[67]   Y. Guo, Y. Sui, J. Zhang, Z. Cai, B. Xu, An all-day solar-driven vapor generator via photothermal and Joule-heating effects, J Mater Chem A Mater. 8 (2020) 25178–25186. https://doi.org/10.1039/D0TA08329A.

[68]   B. Yuan, L. Yang, H. Yang, L. Bai, W. Wang, D. Wei, Y. Liang, H. Chen, Flexible vacancy-mediated MoS2-x nanosheet arrays for solar-driven interfacial water evaporation, photothermal-enhanced photodegradation, and thermoelectric generation, Energy Convers Manag. 252 (2022) 115070. https://doi.org/10.1016/j.enconman.2021.115070.

[69]   K. Li, X. Sun, Y. Wang, J. Wang, X. Dai, G. Li, H. Wang, All-in-one single-piece flexible solar thermoelectric generator with scissored heat rectifying p-n modules, Nano Energy. 93 (2022) 106789. https://doi.org/10.1016/j.nanoen.2021.106789.

[70]   X. Shan, A. Zhao, Y. Lin, Y. Hu, Y. Di, C. Liu, Z. Gan, Low-Cost, Scalable, and Reusable Photothermal Layers for Highly Efficient Solar Steam Generation and Versatile Energy Conversion, Adv Sustain Syst. 4 (2020) 1–8. https://doi.org/10.1002/adsu.201900153.

[71]   Y. Lin, X. Shan, A. Zhao, Y. Hu, Y. Di, C. Liu, Z. Gan, An emerging solar-thermal-electric conversion system based on highly-efficient photothermal nanoabsorber layer, Mater Res Express. 6 (2019) 115531. https://doi.org/10.1088/2053-1591/ab4c4c.

[72]   C.E. Rustana, Sunaryo, S.J. Muchtar, I. Sugihartono, W. Sasmitaningsihhiadayah, A.D.R. Madjid, F.S. Hananto, The Effect of Voltage and Electrode Types on Hydrogen Production from The Seawater Electrolysis Process, J Phys Conf Ser. 2019 (2021) 012096. https://doi.org/10.1088/1742-6596/2019/1/012096.